Three-dimensional ori-kirigami metamaterials with multistability

Yongtao Bai,[1] Shuhong Wang,[1] Xuhong Zhou,[1] and Michael Beer[2]

[1]*School of Civil Engineering, Chongqing University, Chongqing 400045, China*

[2]*Institute for Risk and Reliability, Leibniz Universität Hannover, Hannover 30167, Germany*

Abstract: Ori-kirigami structures offer a good avenue for designing mechanical metamaterials due to their unique advantage of being independent of material properties and scale limitations. Recently, the scientific community has been greatly interested in exploiting the complex energy landscape of ori-kirigami structures to construct multistable systems and play their valuable role in different applications. Here, we present three-dimensional ori-kirigami structures based on generalized waterbomb units, a cylindrical ori-kirigami structure based on waterbomb units, and a conical ori-kirigami structure based on trapezoidal waterbomb units. We investigate the inherent relationships between the unique kinematics and mechanical properties of these three-dimensional ori-kirigami structures and explore their potential usage as mechanical metamaterials that exhibit negative stiffness, snap-through, hysteresis effects, and multistability. What makes the structures even more attractive is their massive folding stroke, where the conical ori-kirigami structure can obtain a huge folding stroke of more than twice its initial height through penetration of its upper and lower boundaries. This study forms the foundation for designing and constructing three-dimensional ori-kirigami metamaterials based on generalized waterbomb units for various engineering applications.

1. Introduction

As carefully constructed artificial structures, either periodic or nonperiodic, the unusual properties of metamaterials are determined by their microstructure rather than composition [1] and are not constrained by the structural scale, which are rarely visible in conventional natural materials. Metamaterials designed to transcend the limitations of conventional material properties have exhibited colorful and exotic properties such as lightweight and high strength [2], negative Poisson's ratio [3], negative compressibility [4], negative stiffness [5], and reprogrammable stiffness [6-8], which have attracted extensive exploration by researchers in the past few years. As a design method to create three-dimensional structures from two-dimensional sheet materials, origami art possesses superior properties such as deployability and reconfigurability independent of model size and material limitations. This geometric design method offers unlimited possibilities for designing and developing new metamaterials.

Rapid developments in computers, mathematics, and geometry have fostered extensive research into the kinematic mechanisms and the mechanical behavior of origami structures. The most popular is the rigid-foldable mode, where the folding motion of rigid origami occurs only at the crease lines and does not involve the deformation of the facets. The relatively simple kinematic mechanisms have attracted tremendous interest from researchers. As a single-degree-of-freedom periodic structure, Miura-ori origami can exhibit the negative Poisson's ratio property of in-plane folding and the positive Poisson's ratio property of out-of-plane bending [9, 10]. Coupling Miura-ori tubes like zippers, Filipov et al. [11] designed a deployable yet stiff origami structure. By studying the motion path of the three-dimensional Tachi-Miura polyhedron, Yang and Yasuda [12] found that the Poisson's ratio can be switched between positive and negative, which is a tunable mechanical property. A generic four-vertex pattern can have up to five stable states under different crease energy distributions [13]. Classical nonrigid origami, including Kresling, Square-twist, and Hypar origami, will have a more complex energy landscape due to the deformation of the facets involved and the highly nonlinear geometric motion, which makes their mechanical behavior more difficult to predict. As a representative of deformable origami, the folding mode of Kresling origami is a compression-torsion coupled motion, and there will be elastic deformation of the facets; Yasuda et al. [14] simplified Kresling origami to a truss model, based on which a structure with tunable stability and stiffness was designed. Under the simplified bar and hinge model, Liu et al. [15] simulated the mechanical behavior of the Hypar pattern and verified the bistable property of the Hypar structure. Based on these exotic and promising properties, origami-inspired metamaterials have been used in different engineering applications, such as biomedical scaffolds [16] and deployable solar panels [17].

Multistable systems can be found in nature [18, 19], and in recent years researchers have worked to create artificial multistable systems and used them for different engineering applications, including energy absorption [20, 21], mechanical switches [22, 23], and actuators [24-26]. Multistable structures can exhibit different mechanical properties by switching between stable states, which supports the development of adaptive structures, such as tunable stiffness [27, 28] and auxetic [29]. Origami structures can use their reconfigurability to provide a flexible platform for achieving multistability.

In this study we adopt three-dimensional ori-kirigami structures as a building block of mechanical metamaterials to achieve simultaneous rigid foldability and structural multistability. Specifically, these three-dimensional ori-kirigami structures are cylindrical and conical ori-kirigami metamaterials based on generalized waterbomb units. By exploring the mechanical properties of the cylindrical and conical ori-kirigami structures, we found that the structures have multistable characteristics, which means they can maintain two or more different folding configurations. In addition, we can observe negative stiffness, snap-through, and hysteresis effects in their mechanical responses, which are achieved in elastic systems using mechanical instabilities so that such mechanical responses are reversible and repeatable. The conventional cylindrical and conical origami structures usually consist of generalized waterbomb units tessellated and stacked sequentially [30, 31]. However, these origami structures cannot be rigid-foldable, which has led to minimal research and application due to not possessing the most significant feature (rigid-foldable) of origami structures. To break through this limitation, we cut two waterbomb units on the same layer along the adjacent boundary to form cylindrical and conical ori-kirigami structures [see Figs. 1(a) and 2(a)] to satisfy the rigid foldability (i.e., deformation occurs only at the crease lines). In order to connect the split waterbomb units to form a whole, we can set up a connection structure at both ends [Figs. 1(a) and 2(a)]. Compared with other origami-based three-dimensional structures [32, 33], the conical ori-kirigami structure has a unique feature: its upper and lower boundaries can penetrate. This implies that we can obtain a considerable folding stroke over twice its initial height, which will provide new ideas for designing structures such as actuators and impact energy absorbers. The conical ori-kirigami structure can exhibit multistable properties under the premise that penetration can occur of its upper and lower boundaries, which is better than those three-dimensional origami structures that have to be multistable by adjusting the crease stiffness and zero potential energy states [34, 35]. It is worth noting that self-folding structures based on origami have recently received much attention from engineers. From the micro- to macroscale range, by combining with current smart materials, driving methods have been designed that rely on chemical environment [36], temperature [37], and light [38] to achieve self-folding. For example, using thermal fluctuations as a driving force can make polyhedral nets fold to target three-dimensional geometries [39, 40]. Unlike these systems that require a continuous supply of energy to complete self-folding, multistable structures only need to provide energy to initiate switching between stable states to achieve reconfigurable performance.

The rest of the paper is organized as follows. Section II presents the geometric design and folding kinematics of these three-dimensional ori-kirigami structures based on generalized waterbomb units. Based on the discussion provided in Sec. II, Sec. III investigates the force-displacement relationships of the three-dimensional ori-kirigami structures. Finally, Sec. IV presents the important conclusions.

2. Kinematic analysis

2.1 The cylindrical ori-kirigami structure

First, we describe the geometric features and kinematic mechanisms of the cylindrical ori-kirigami structure based on the waterbomb units. The side and top views of the cylindrical ori-kirigami cell are shown in Figs. 1(a) and 1(b), respectively. n_w is the number of waterbomb units contained in a cylindrical ori-kirigami cell [i.e., $n_w = 6$ for Fig. 1(a)], and all waterbomb units form a whole through the connecting segments at both ends [Fig. 1(a)]. The geometry of each waterbomb unit can be characterized by a length parameter (b) and an acute angle (α) [see Fig. 1(c)]. As shown in Fig. 1(c), the foldable spreading point G is located at the center of the origami unit, and points C and D are located at the two vertical edges and pass through the central axis of the unit [dashed line in Fig. 1(c)]. Accordingly, the height (H) of the cylindrical ori-kirigami cell corresponds to the distance between crease lines AB and EF along the z-axis, and the size of the connecting segments can be ignored because they do not deform during the folding process. The axial displacement u is used to express deformations of the structure and can be calculated as $u = H_{(0)} - H$, where $H_{(0)}$ is the height of the cylindrical ori-kirigami cell when the gap between two adjacent waterbomb units is closed. Each waterbomb unit maintains the same motion characteristics during the folding of the cylindrical ori-kirigami cell along the z-axis, so we can understand the rigid folding characteristics of the cylindrical ori-kirigami cell by analyzing individual waterbomb unit, as shown in the blue (dark gray) area in Fig. 1.

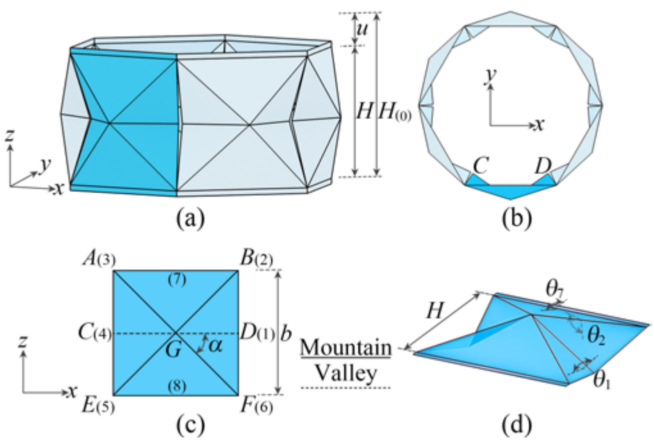

FIG. 1 (a) Side view of the cylindrical ori-kirigami cell; (b) Top view of the cylindrical ori-kirigami cell; (c) The crease pattern of the waterbomb unit with mountain and valley folds; (d) Folded configuration of the waterbomb unit corresponding to the blue (dark gray) areas in (a) and (b). There are eight crease lines, and each crease line is assigned a number. θ_i ($i=1,2,\cdots,6$) is the dihedral angle at crease line *i*. θ_7 and θ_8 are the waterbomb unit's boundary crease folding angles related to the *z*-axis.

The kinematic mechanisms of the origami structures can generally be described by the folding angle at each crease line, as shown in Fig. 1(d). Each waterbomb unit has only three folding angle parameters due to the symmetry condition, which are the folding angles θ_1 ($\theta_4=\theta_1$), θ_2 ($\theta_3=\theta_5=\theta_6=\theta_2$), and θ_7 ($\theta_8=\theta_7$, θ_7 is the complementary angle of the angle between the facet *AGB* and the *z*-axis), and they are functions for α, *b* (determined by the given geometry) and the height *H* (which varies with the degree of folding) of the cylindrical ori-kirigami cell. The mathematical expressions for these folding angles can be obtained according to the necessary conditions designed by Belcastro and Hull [41] for the foldability of single-vertex origami. For a single vertex with *j* crease lines, the angle variation constraint for these folding angles ($\rho_1,\cdots,\rho_j$) can be given by the following equation:

$$R(\rho_1,\cdots,\rho_j)=\chi_1\cdots\chi_{j-1}\chi_j=\mathbf{I} \tag{1}$$

where χ_i is the rotation matrix around the crease line *i*, the expression of χ_i as:

$$\chi_i=\begin{bmatrix}1 & 0 & 0\\ 0 & \cos\rho_i & -\sin\rho_i\\ 0 & \sin\rho_i & \cos\rho_i\end{bmatrix}\begin{bmatrix}\cos\omega_i & -\sin\omega_i & 0\\ \sin\omega_i & \cos\omega_i & 0\\ 0 & 0 & 1\end{bmatrix} \tag{2}$$

Where ω_i is the angle between crease lines *i* and *i*+1 (when *i*+1>*j*, take *i*+1 as 1); ρ_i is the complementary angle of the dihedral angle at crease line *i*, and assign positive and negative values to the valley and mountain folds, respectively.

In the waterbomb unit shown in Fig. 1(c), the angles between adjacent crease lines are $\omega_1 = \omega_3 = \omega_4 = \omega_6 = \alpha$ and $\omega_2 = \omega_5 = \pi - 2\alpha$. During the folding of the waterbomb unit in the *z*-direction, the folding angle at each fold have the following relationships: $\rho_2 = \rho_3 = \rho_5 = \rho_6$, $\rho_1 = \rho_4$. Substituting them into Eq. (1), we can obtain

$$\tan\rho_2 = \frac{2\cos\alpha\sin\rho_1}{1-\cos^2\alpha\cos\rho_1 - \cos^2\alpha - \cos\rho_1} \tag{3}$$

Substituting the relationships ($\rho_1 = \pi - \theta_1$, $\rho_2 = \theta_2 - \pi$) between the folding angle ρ_i at crease line *i* and the dihedral angle θ_i into Eq. (3), we obtain

$$\theta_2 = \begin{cases} \pi + \arctan\dfrac{2\cos\alpha\sin\theta_1}{\cos^2\alpha\cos\theta_1 - \cos^2\alpha + \cos\theta_1 + 1} & \theta_1 \geq \arccos\dfrac{\cos^2\alpha - 1}{\cos^2\alpha + 1} \\ \arctan\dfrac{2\cos\alpha\sin\theta_1}{\cos^2\alpha\cos\theta_1 - \cos^2\alpha + \cos\theta_1 + 1} & \theta_1 < \arccos\dfrac{\cos^2\alpha - 1}{\cos^2\alpha + 1} \end{cases} \tag{4}$$

Additionally, we can obtain expressions of θ_1 and θ_7 in terms of *H* (the height of the cylindrical ori-kirigami cell) as follows:

$$\theta_1 = 2\arcsin\frac{H}{b}, \quad \theta_7 = \frac{\pi}{2} + \arcsin\frac{H}{b} = \frac{\pi + \theta_1}{2} \tag{5}$$

As mentioned above, in the folding process of the cylindrical ori-kirigami cell, all folding angles can be described by the dihedral angle θ_1 of crease line 1 as an independent variable so that the folding configuration of the cylindrical ori-kirigami cell can be uniquely determined at different *H*. Therefore, the folding of the cylindrical ori-kirigami cell in the z-direction is a single-degree-of-freedom mechanism. Note that the waterbomb unit can be completely flat-foldable when α is less than or equal to 45°. When it is greater than 45°, points *C* and *D* will collide before being completely flat-folded, resulting in a self-locking state of the waterbomb unit. The geometric characteristics of the waterbomb unit under this state and the folding angle at each fold are described in the Supplemental Material.

2.2 The conical ori-kirigami structure

Next, we describe the geometric features and kinematic mechanisms of the conical ori-kirigami cell, which is based on the trapezoidal waterbomb units. The side and top views of the conical ori-kirigami cell are shown in Figs. 2(a) and 2(b), respectively. The conical ori-kirigami cell consists of n_{tw} [i.e., $n_{tw} = 6$ for Fig. 2(a)] trapezoidal waterbomb units, and all the trapezoidal waterbomb units form a whole through the connecting segments at both ends [Fig. 2(a)]. The geometry of each trapezoidal waterbomb unit can be characterized by four length parameters (a_1, a_2, l_1, l_2) [Fig. 2(c)]. As shown in Fig. 2(c), the foldable spreading point G' is located on the mid-pipeline of the origami unit; the valley folds $G'D'$ and $G'C'$ are perpendicular to the corresponding side edges in the trapezoidal waterbomb unit, respectively. Each trapezoidal waterbomb unit maintains the same motion characteristics during the folding of the conical ori-kirigami cell in the *z*-direction, so we can characterize the shape of the conical ori-kirigami cell by defining its height (H', the distance between crease lines $A'B'$ and $E'F'$ along the *z*-axis). Letting $H'_{(0)}$ be the height of the conical ori-kirigami cell when the gap between two adjacent trapezoidal waterbomb units is closed, we can express deformations of the structure by axial displacement $u' = H'_{(0)} - H'$ where compression is defined to be positive. Accordingly, we can understand the rigid folding characteristics of the conical ori-kirigami cell by analyzing individual trapezoidal waterbomb unit [as shown in the blue (dark gray) area in Fig. 2].

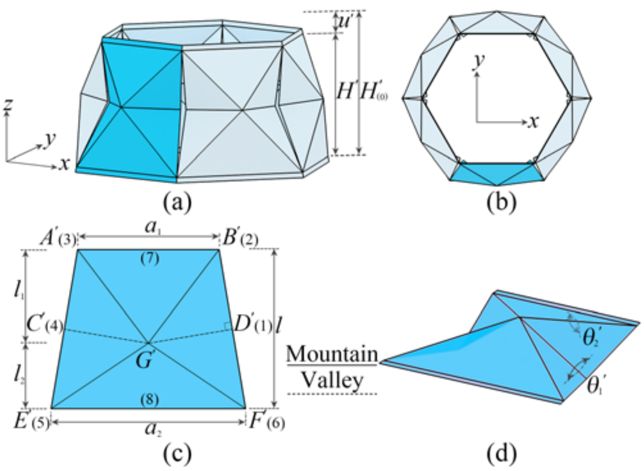

FIG. 2 (a) Side view of the conical ori-kirigami cell; (b) Top view of the conical ori-kirigami cell; (c) The crease pattern of the trapezoidal waterbomb unit with mountain and valley folds; (d) Folded configuration of the trapezoidal waterbomb unit corresponding to the blue (dark gray) areas in (a) and (b). There are eight crease lines, and each crease line is assigned a number. θ_i ($i = 1, 2, \cdots, 6$) is the dihedral angle at crease line *i*. θ_7 and θ_8 are the trapezoidal waterbomb unit's boundary crease folding angles related to the z-axis.

As shown in Figs. 2(c) and 2(d), each trapezoidal waterbomb unit has a total of five folding angle parameters due to the symmetry condition, namely the folding angles θ_1' ($\theta_4' = \theta_1'$), θ_2' ($\theta_3' = \theta_2'$), θ_6' ($\theta_5' = \theta_6'$), θ_7' and θ_8'. By changing the geometric parameters of the trapezoidal waterbomb unit, a total of seven final folding cases can be generated, including two cases that can be completely flat-foldable and five cases with self-locking angles (see the Supplementary Material for details). To conveniently analyze the kinematics of the conical ori-kirigami cell, we specify $l_1 = l_2$, so that the trapezoidal waterbomb unit can only produce three final folding cases. Two of these three folding cases have a self-locking angle ($\overline{\theta'}$), defined as the dihedral angle between the facet $A'G'B'$ and the facet $E'G'F'$ when self-locking occurs, and the formula for calculating the self-locking angle is shown in the Supplementary Material.

Due to a large number of geometric parameters for the trapezoidal waterbomb unit, to conveniently analyze the kinematics and the force-displacement relationship of the conical ori-kirigami cell, here we define l and a_1 be the variables with parameter a_2, where $l = \xi a_2$, $a_1 = \eta a_2$ ($\eta < 1$). First let's get the expression for θ_1', the conical ori-kirigami cell is shown in Fig. 3.

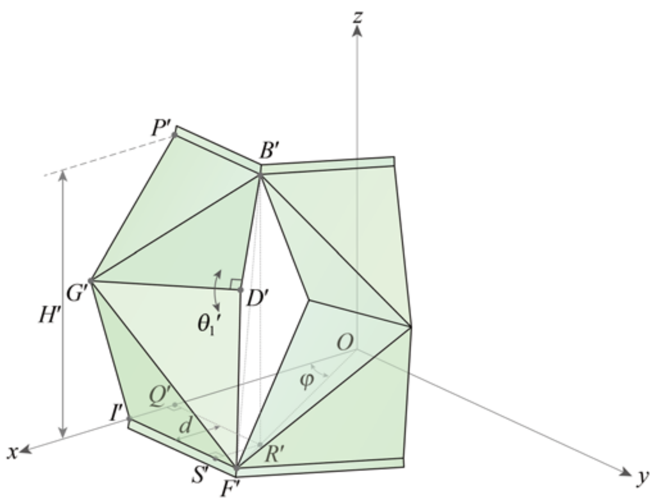

FIG. 3 Folded configuration of the conical ori-kirigami cell ($1/n_{tw}$).

We can calculate the distance between the points B' and F' as

$$l_{\overline{B'F'}} = \sqrt{H'^2 + d^2 + l_{S'F'}{}^2} \tag{6}$$

where

$$d = l_{I'O} - l_{Q'O} = \frac{a_2}{2\tan\pi/n_{tw}} - \frac{a_1}{2\tan\pi/n_{tw}}$$
$$l_{S'F'} = \frac{a_2 - a_1}{2} \tag{7}$$

Then, we can calculate θ_1' as

$$\theta_1' = \arccos\frac{l_{B'D'}^2 + l_{F'D'}^2 - l_{\overline{B'F'}}^2}{2l_{B'D'}l_{F'D'}} \tag{8}$$

where $l_{B'D'}$ and $l_{F'D'}$ are calculated as detailed in the Supplemental Material, $l_{\overline{B'F'}}$ is calculated from Eq. (6).

We only discuss the first final folding state (see Supplemental Material for details) here in order to facilitate the analysis of the variation relationship between θ_2', θ_6' and θ_1'. The subsequent analysis of the force-displacement response for the conical ori-kirigami structure will be based on the first final folding case. For the first final folding case, the geometric condition of the trapezoidal waterbomb unit needs to satisfy $l_1 = l_2 = l_{G'D'}$ [see Fig. S4(a) and Eq. (S17) in the Supplemental Material for details], we can obtain

$$\xi = \sqrt{\eta} \tag{9}$$

For the first final folding case, the angle between the adjacent crease lines of the trapezoidal waterbomb unit shown in Fig. 2(c) has the following relationship:

$$\omega_2' = \omega_1' + \omega_3' = 2\omega_1'$$
$$\omega_5' = \omega_4' + \omega_6' = 2\omega_6' \tag{10}$$

Since the sum of the angles between all adjacent crease lines connecting a single vertex is 2π, we can obtain

$$\omega_1' + \omega_6' = \frac{\pi}{2} \tag{11}$$

In the first final folding case, we assume that the geometric parameters of the trapezoidal waterbomb unit are

$$\omega_1' = \omega_3' = \beta,\ \omega_2' = 2\beta,\ \omega_4' = \omega_6' = \frac{\pi}{2} - \beta,\ \omega_5' = \pi - 2\beta \tag{12}$$

According to the symmetry condition, there are relationships between the folding angle at each crease line during the folding of the conical ori-kirigami cell along the *z*-direction as

$$\rho_1' = \rho_4',\ \rho_2' = \rho_3',\ \rho_5' = \rho_6' \tag{13}$$

Substituting Eqs. (12) and (13) into Eq. (1), we can obtain

$$\begin{gathered}
\tan\rho_2' = \frac{2\cos^2\rho_1'\sin^2\beta - \cos^2\rho_1' - 2\sin^2\beta + 1}{\sin\rho_1'(\cos\rho_1'\cos\beta\sin^2\beta + \cos\rho_1'\sin^3\beta - \cos\beta\sin^2\beta - \sin^3\beta - \cos\rho_1'\cos\beta + \sin\beta)} \\
\rho_2' = \rho_6'
\end{gathered} \tag{14}$$

Substituting the relationships ($\rho_1' = \pi - \theta_1'$, $\rho_2' = \theta_2' - \pi$, $\rho_6' = \theta_6' - \pi$) between the folding angle ρ_i' at crease line *i* and the dihedral angle θ_i' into Eq. (14), we obtain

$$\begin{gathered}
\theta_2' = \begin{cases}
\pi + \arctan\dfrac{2\cos^2\theta_1'\sin^2\beta - \cos^2\theta_1' - 2\sin^2\beta + 1}{\sin\theta_1'\begin{pmatrix} -\cos\theta_1'\cos\beta\sin^2\beta - \cos\theta_1'\sin^3\beta \\ -\cos\beta\sin^2\beta - \sin^3\beta + \cos\theta_1'\cos\beta + \sin\beta \end{pmatrix}} & \theta_1' \geq \pi - \arccos\dfrac{\sin\beta\cos\beta}{\sin\beta\cos\beta + 1} \\
\arctan\dfrac{2\cos^2\theta_1'\sin^2\beta - \cos^2\theta_1' - 2\sin^2\beta + 1}{\sin\theta_1'\begin{pmatrix} -\cos\theta_1'\cos\beta\sin^2\beta - \cos\theta_1'\sin^3\beta \\ -\cos\beta\sin^2\beta - \sin^3\beta + \cos\theta_1'\cos\beta + \sin\beta \end{pmatrix}} & \theta_1' < \pi - \arccos\dfrac{\sin\beta\cos\beta}{\sin\beta\cos\beta + 1}
\end{cases} \\
\theta_6' = \theta_2'
\end{gathered} \tag{15}$$

As mentioned above, the folding angles at all folds of the trapezoidal waterbomb unit under $\xi = \sqrt{\eta}$ can be described by the dihedral angle θ_1' of crease line 1 as an independent variable. Therefore the folding of each trapezoidal waterbomb unit along the z-axis is a single-degree-of-freedom mechanism. While folding the conical ori-kirigami cell along the *z*-direction, we can consider the facets $A'G'B'$ and $E'G'F'$ as a linkage mechanism composed of $G'P'$ and $G'I'$ as shown in Fig. 4. Assume that the linkage $G'I'$ is in a circular motion around the point I' on a fixed circle of radius l_2, while the linkage $G'P'$ is constantly in motion on a movable circle of radius l_1 and centered at the point P'.

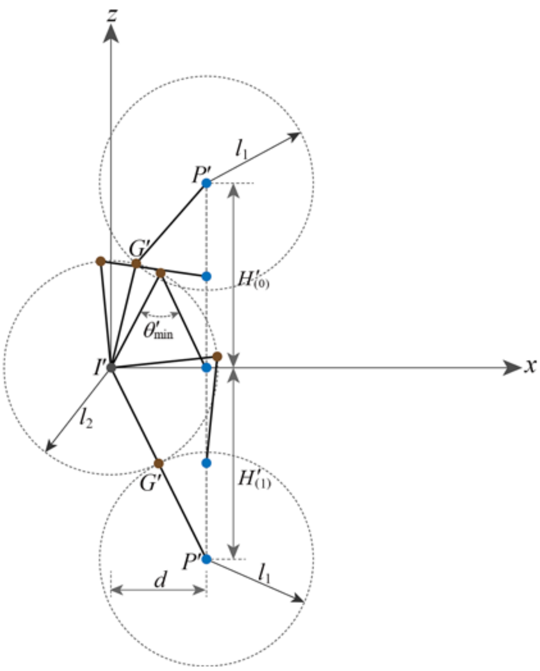

FIG. 4 The folding motion mechanism of the conical ori-kirigami cell. There are four configurations of the conical ori-kirigami cell during folding along the z-axis. The facets $A'G'B'$ and $E'G'F'$ can be considered as a linkage mechanism connected by point G'. Assuming that point I' is not moving; point P' is always moving on the $x=d$ axis. $H'_{(0)}$ is the height of the structure when the gap between two adjacent trapezoidal waterbomb units is closed, and $H'_{(1)}$ is the height of the structure when the gap is closed again. $\theta'_{\min}$ is the minimum dihedral angle between the facets $A'G'B'$ and $E'G'F'$.

As shown in Fig. 5, we define θ_7' and θ_8' as the angle between $G'P'$, $G'I'$ and the z-axis, respectively.

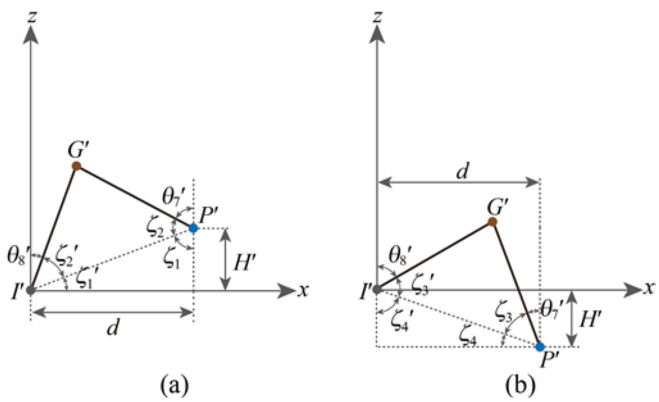

FIG. 5 Calculation schematic of the folding angle for crease lines 7 and 8.

During the folding process of the conical ori-kirigami cell in the z-direction, before the point P'

does not cross the x-axis (Fig. 5(a)), we can obtain

$$\zeta_1 = \arccos\frac{H'}{l_{\overline{P'T'}}},\ \zeta_1' = \arcsin\frac{H'}{l_{\overline{P'T'}}},\ \zeta_2 = \zeta_2' = \arccos\frac{l_{\overline{P'T'}}}{2l_{G'P'}} \tag{16}$$

where

$$l_{\overline{P'T'}} = \sqrt{d^2 + H'^2} \tag{17}$$

Therefore, we can obtain the expressions for θ_7' and θ_8' in this case as

$$\begin{aligned} \theta_7' &= \pi - (\zeta_1 + \zeta_2) \\ \theta_8' &= \frac{\pi}{2} - (\zeta_1' + \zeta_2') \end{aligned} \tag{18}$$

After the point P' cross the x-axis (Fig. 5(b)), we can obtain

$$\zeta_4 = \arcsin\frac{H'}{l_{\overline{P'T'}}},\ \zeta_4' = \arccos\frac{H'}{l_{\overline{P'T'}}},\ \zeta_3 = \zeta_3' = \arccos\frac{l_{\overline{P'T'}}}{2l_{G'P'}} \tag{19}$$

Finally, we can obtain the expressions for θ_7' and θ_8' in this case as

$$\begin{aligned} \theta_7' &= \frac{\pi}{2} - (\zeta_3 + \zeta_4) \\ \theta_8' &= \pi - (\zeta_3' + \zeta_4') \end{aligned} \tag{20}$$

It is noteworthy that the dihedral angle between the facet $A'G'B'$ and the facet $E'G'F'$ of each trapezoidal waterbomb unit decreases before the penetration of the upper and lower boundaries in the conical ori-kirigami cell. Furthermore, it increases after the penetration during the folding of the conical ori-kirigami structure along the z-direction. Therefore, the dihedral angle between the facet $A'G'B'$ and the facet $E'G'F'$ reaches a minimum at the critical position when the upper and lower boundaries of the conical ori-kirigami cell are penetrated. The minimum dihedral angle $\theta'_{\min}$ can be calculated as

$$\theta'_{\min} = \arccos\frac{l_1^2 + l_2^2 - d^2}{2l_1 l_2} = \arccos\left\{\frac{(2\xi^2 + \eta^2 - 2\eta + 1)\cos^2\dfrac{\pi}{n_{tw}} - 2\xi^2}{2(\cos^2\dfrac{\pi}{n_{tw}} - 1)\xi^2}\right\} \tag{21}$$

In order to ensure the penetration of the upper and lower boundaries of the conical ori-kirigami cell, the minimum dihedral angle ($\theta'_{\min}$) between the facet $A'G'B'$ and facet $E'G'F'$ must be greater than or equal to the self-locking angle ($\overline{\theta'}$) of the trapezoidal waterbomb unit. The analytical contour plot of the self-locking angle of the trapezoidal waterbomb unit as a function of continuous η and ξ is shown in Fig. 6(a). Only the geometric conditions on the white dashed line can ensure the completely flat-foldability of the trapezoidal waterbomb unit. The insets show the three final folding configurations of the trapezoidal waterbomb unit under $l_1 = l_2$. Figure 6(b) shows the contour plot of the minimum dihedral angle between facets $A'G'B'$ and $E'G'F'$ during the folding of the conical ori-kirigami cell. The geometric conditions in the area ($\theta'_{\min} > \overline{\theta'}$) enclosed by the two white dashed lines and the coordinate axis can satisfy the penetrability of the upper and lower boundaries of the conical ori-kirigami cell.

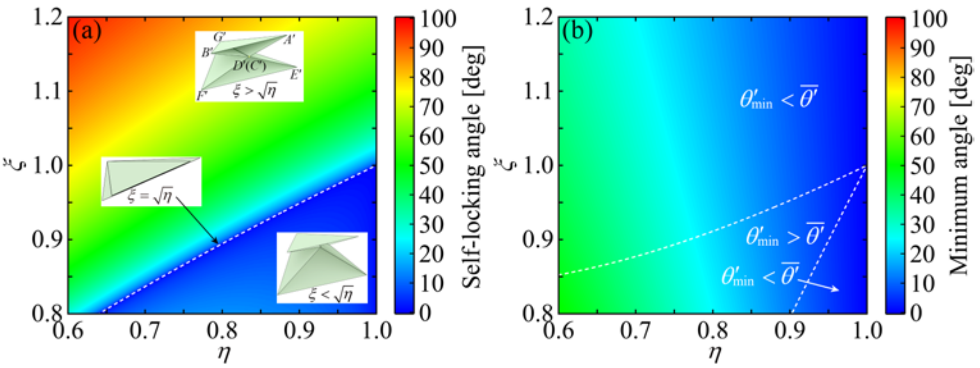

FIG. 6 (a) Contour plot of the self-locking angle as a function of η and ξ for the trapezoidal waterbomb unit under $l_1 = l_2$. Insets show the three folding configurations of the trapezoidal waterbomb unit under self-locking state. (b) Contour plot of the minimum angle between the facets $A'G'B'$ and $E'G'F'$ during the folding of the conical ori-kirigami cell under $l_1 = l_2$.

3. Analysis of force-displacement relationship

We now investigate the relationships between the force and the degree of folding to validate the multistable nature of the ori-kirigami structures. We assume that the structures are rigid-foldable, i.e., the facets remain rigid during folding and are connected by elastic hinges with prescribed torsional stiffness. This modeling approach is simple and effective [42-44], such that the following equation can determine the total elastic potential energy stored in the origami unit,

$$\Pi = \frac{1}{2}\sum_{i=1}^{N} K_i(\theta_i - \theta_i^0)^2 \tag{22}$$

where N is the number of crease lines contained in the origami unit, K_i is the torsional stiffness constant at fold i, and θ_i^0 is the initial folding angle when fold i is at zero potential energy. To analyze the mechanical properties of the ori-kirigami structures, we considered two cases accounting for (N = 8) and not accounting for (N = 6) the deformation of boundary creases between the origami units and connecting segments (see Fig. 7).

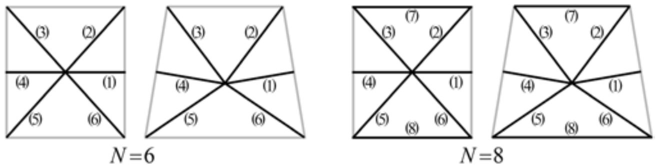

FIG. 7 The two cases for analyzing the mechanical properties of the ori-kirigami structures. The black crease lines are considered, and each crease line is assigned a number.

3.1 The cylindrical ori-kirigami structure

We specify the torsional stiffness per unit length for the creases in the waterbomb unit as k, so K_i in Eq. (24) can be calculated as $K_i = kL_i$ (L_i is the length of crease i). Applying the principle of virtual work to the geometry of the waterbomb unit, the required compression force along the z axis of the cylindrical ori-kirigami cell with n_w = 6 can be obtained as [see Eqs. (S6)–(S13) in the Supplemental Material]

$$\frac{F\big|_{N=8}}{k} = -\frac{2n_w}{\tan\alpha\cos\dfrac{\theta_1}{2}}\left\{(\theta_1-\theta_1^0)-\frac{4(\theta_2-\theta_2^0)}{\cos^2\alpha\cos\theta_1-\cos^2\alpha-\cos\theta_1-1}+(\theta_7-\theta_7^0)\right\} \tag{22}$$

Here we eliminate the effect of stiffness factor and waterbomb unit size by a normalized force. Figure 8 shows the relationship between the force along the z axis of the cylindrical ori-kirigami cell (n_w = 6) and the folding ratio under different initial conditions. The folding ratio we define as $(H_{(0)} - H)/H_{(0)}$, where $H_{(0)}$ is the height of the cylindrical ori-kirigami cell when the gap between two adjacent waterbomb units is closed. The geometric characteristics of the waterbomb unit under $H = H_{(0)}$ and the folding angle at each fold are described in the Supplemental Material. The black curve in Fig. 8 shows the force-folding ratio relationship considering only the folding deformation of the six folds intersecting at point G in the waterbomb unit, i.e., the torsional stiffness of the boundary folds 7 and 8 is considered zero. In the case of $\theta_1^0 = \theta_1^{(0)}$ ($\theta_1^{(0)}$ is the folding angle corresponding to $H_{(0)}$ at fold 1), we observe a valley load ($F_{\min}$) greater than zero and a negative stiffness region (between peak load and valley load) in the force-folding ratio relationship for the cylindrical ori-kirigami cell with or without considering the boundary folds deformation at α = 48° and α = 49° (the waterbomb unit has a self-locking state), respectively.

Physically, a slight perturbation near the critical state under load control can cause the structure to undergo snap-through or snap-back, resulting in hysteresis effects due to the noncoincident loading-unloading path. After unloading, the structure automatically returns to its initial state, so this mechanical response is reversible and repeatable.

The cylindrical ori-kirigami cells can also be massively expanded in the plane with a certain regularity and then vertically connected in series to construct multilayer cellular metamaterials (see Figs. S10 and S11 in the Supplemental Material for details). By analyzing the force-displacement relationship of cellular structure based on two layers of cylindrical ori-kirigami cells, we find that such structures have similar mechanical properties compared to a single cell. Compared to the single-layer structure, under specific geometric conditions (α = 48°, N = 6), the force-displacement relationship of the two-layer cellular structure will have two negative stiffness regions since the structure will enter the instability state layer by layer. The structure then undergoes successive snap-through or snap-back and produces hysteresis effects (see Fig. S13 in the Supplemental Material).

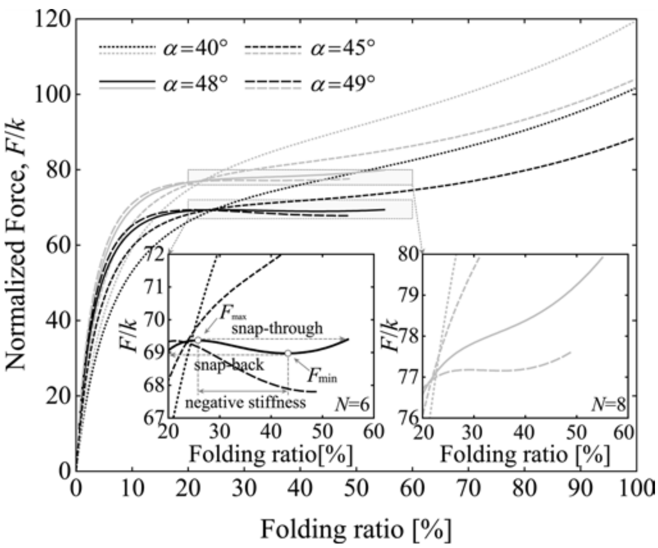

FIG. 8 Force-folding ratio relationship of the cylindrical ori-kirigami cell when n_w (number of the waterbomb unit) is 6, and the initial folding angle is $\theta_1^0 = \theta_1^{(0)}$. The two insets each show an enlarged view of the shaded regions. The black and gray lines show the force-displacement relationships of the conical ori-kirigami cell at N = 6 and N = 8, respectively.

3.2 The conical ori-kirigami structure

Next, we investigate the force-folding ratio relationship of the conical ori-kirigami structure under

$l_1 = l_2$ and $\xi = \sqrt{\eta}$. Here we specify k' as the torsional stiffness per unit length of all the folds in the trapezoidal waterbomb unit. The calculations of the required force in the z direction for the conical ori-kirigami cell are described by Eqs. (S30)–(S34) in the Supplemental Material. Figures 9(a) and 9(b) show the force-folding ratio relationship of the conical ori-kirigami cell under $l_1 = l_2$ and $\xi = \sqrt{\eta}$. Here, the folding ratio is defined as either $(H'_{(0)} - H')/H'_{(0)}$ (before the penetration of the upper and lower boundaries in the conical ori-kirigami cell) or $(H'_{(0)} + H')/H'_{(0)}$ (after penetration), where $H'_{(0)}$ is the height of the conical ori-kirigami cell when the gap between two adjacent trapezoidal waterbomb units is closed, and the geometry of the trapezoidal waterbomb unit and the folding angle at each crease line in this case are described in the Supplemental Material. When the initial folding angle $\theta_1'^{0}$ is $\theta_1'^{(0)}$ ($\theta_1'^{(0)}$ is the folding angle corresponding to $H'_{(0)}$ at fold 1), we observe that the conical ori-kirigami cell with η = 0.8 and n_{tw} = 6 has two stable configurations [see the black solid curve in Fig. 9(a)], without considering the folding deformation of the boundary folds 7 and 8, one is the initial state (folding ratio of 0%) and the other is close to the final folding state (folding ratio of 200%).

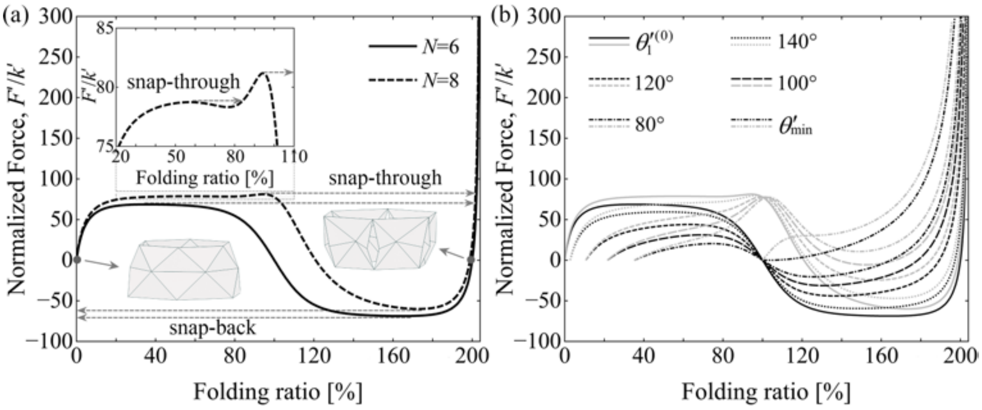

FIG. 9 Force-folding ratio relationship of the conical ori-kirigami cell with η = 0.8 and n_{tw} = 6. (a) The initial folding angle is $\theta_1'^{0} = \theta_1'^{(0)}$. Insets indicate the stable configurations of the conical ori-kirigami cell and an enlarged view of the shaded regions. (b) The black and gray lines show the force-displacement relationships of the conical ori-kirigami cell under different initial angles at N = 6 and N = 8, respectively.

An interesting phenomenon is that all the trapezoidal waterbomb units in the conical ori-kirigami cell have the same folding state in both stable states, except that the foldable spreading points G'

of all the trapezoidal waterbomb units point to the outside of the conical ori-kirigami cell in the first stable state, while they point to the inside of the conical ori-kirigami cell in the second stable state. In addition, there is a valley load less than zero in the force-folding ratio relationship and a negative stiffness region, where snap-through or snap-back occurs in the critical state under load control and produces hysteresis effects. After unloading, the structure stays in the second stable state and can only be passively restored to the initial state by applying a load in the opposite direction.

When we consider the folding deformation of the boundary folds, we can find from the force-folding ratio relationship of the conical ori-kirigami cell that it is still a bistable system [see the black dashed line in Fig. 9(a), where there are two points with positive slope and zero force]. An interesting phenomenon is two negative stiffness regions in its force-folding ratio relationship, so snap-through will occurs twice under load control. It is worth noting that a load increase process is required between these two snap-throughs. Both conditions of the conical ori-kirigami cell can produce negative stiffness, snap-through, and hysteresis phenomena that have potential applications in impact isolation and energy absorption. These complex mechanical responses are due to the highly nonlinear relationship between the folding angle and the folding ratio of the conical ori-kirigami structure (see Fig. 10). The strongly nonlinear relationship plays a crucial role in the multistable properties of the conical ori-kirigami structure. Under specific geometrical and folding configurations, the conical ori-kirigami cell can exhibit five different equilibrium states under the same normalized force (see Fig. S8 in the Supplemental Material).

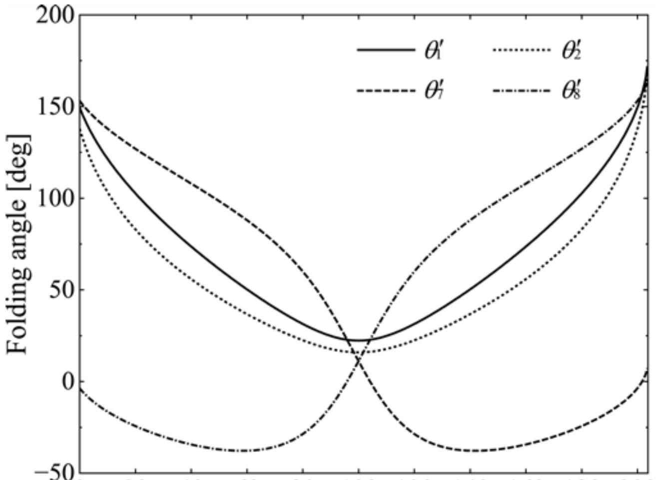

FIG. 10 The relationship between the folding angle and the folding ratio of the conical ori-kirigami cell with η = 0.8 and n_{tw} = 6.

We now investigate the force-folding ratio relationship of the conical ori-kirigami cell under different initial folding angles [see Fig. 9(b)]. We can observe that the conical ori-kirigami cell with η = 0.8 and n_{tw} = 6 can exhibit monostable or bistable states at appropriate initial folding angles, which means that the stability of the conical ori-kirigami structure can be artificially manipulated by changing $\theta_1'^0$. It is noteworthy that the stability does not rely on material properties but is achieved by the kinematics of this structure. Moreover, the multistability property can provide self-locking mechanisms, so that the structure can cease its folding motion and maintain a specific folding configuration stably.

Unlike the cylindrical ori-kirigami cell, the conical ori-kirigami cell can only be expanded vertically in series into a multilayer metamaterial structure (see Supplemental Material for details). With an energy-based mechanical analysis approach, we investigate the mechanical properties of the two-layer conical ori-kirigami structure, which we can observe from its potential energy paths to possess four stable configurations (see Figs. S15 and S16 in the Supplemental Material for details). After careful design, the two-layer conical ori-kirigami structure can complete the whole folding stroke smoothly during loading and unloading, i.e., the layers of conical ori-kirigami cells do not collide during the folding process. An interesting phenomenon is that the structure can be folded under displacement control during loading and unloading following independent motion paths. Each path connects only three stable configurations and goes through one complete loading and unloading cycle to traverse the four stable configurations. The loading and unloading paths do not overlap and thus produce hysteresis effects, which is a different mechanism from the hysteresis effects that occur with snap-through and snap-back under load control.

4. Summary

In summary, we investigated the unique kinematic and mechanical properties of cylindrical and conical ori-kirigami structures based on generalized waterbomb units. We found that these three-dimensional ori-kirigami structures can exhibit negative stiffness, snap-through, hysteresis effects, and multistability, and these mechanical responses are reversible and repeatable. At the same time, compared with the conventional three-dimensional origami structures, the upper and lower boundaries of the conical ori-kirigami structure can be penetrated to obtain a substantial folding stroke over twice its initial height. The results of this study can provide ideas for the construction and design of three-dimensional mechanical metamaterials with greater degrees of freedom and controllable structural stability, which will show great potential for various engineering applications such as space structures, actuators, and energy absorbers.

ACKNOWLEDGMENT

We acknowledge support from the National Key R&D Program of China under Grant No. 2022YFB2602700 and the National Natural Science Foundation of China under Grant No. 21FAA03167.

References

[1] M. Kadic, T. Bückmann, R. Schittny, M. Wegener, Metamaterials beyond electromagnetism, Reports on Progress in physics, 76 (2013) 126501.

[2] T.A. Schaedler, A.J. Jacobsen, A. Torrents, A.E. Sorensen, J. Lian, J.R. Greer, L. Valdevit, W.B. Carter, Ultralight metallic microlattices, Science, 334 (2011) 962-965.

[3] J.N. Grima, K.E. Evans, Auxetic behavior from rotating squares, (2000).

[4] Z.G. Nicolaou, A.E. Motter, Mechanical metamaterials with negative compressibility transitions, Nat Mater, 11 (2012) 608-613.

[5] X. Tan, S. Chen, S. Zhu, B. Wang, P. Xu, K. Yao, Y. Sun, Reusable metamaterial via inelastic instability for energy absorption, International Journal of Mechanical Sciences, 155 (2019) 509-517.

[6] S. Li, H. Fang, K. Wang, Recoverable and programmable collapse from folding pressurized origami cellular solids, Physical review letters, 117 (2016) 114301.

[7] Z. Zhai, Y. Wang, H. Jiang, Origami-inspired, on-demand deployable and collapsible mechanical metamaterials with tunable stiffness, Proceedings of the National Academy of Sciences, 115 (2018) 2032-2037.

[8] X. Zhou, S. Zang, Z. You, Origami mechanical metamaterials based on the Miura-derivative fold patterns, Proceedings of the Royal Society A: Mathematical, Physical and Engineering Sciences, 472 (2016) 20160361.

[9] M. Schenk, S.D. Guest, Geometry of Miura-folded metamaterials, Proceedings of the National Academy of Sciences, 110 (2013) 3276-3281.

[10] Z.Y. Wei, Z.V. Guo, L. Dudte, H.Y. Liang, L. Mahadevan, Geometric Mechanics of Periodic Pleated Origami, Physical Review Letters, 110 (2013).

[11] E.T. Filipov, T. Tachi, G.H. Paulino, Origami tubes assembled into stiff, yet reconfigurable structures and metamaterials, Proceedings of the National Academy of Sciences, 112 (2015) 12321-

12326.
[12] H. Yasuda, J. Yang, Reentrant origami-based metamaterials with negative Poisson's ratio and bistability, Physical review letters, 114 (2015) 185502.
[13] S. Waitukaitis, R. Menaut, B.G.-g. Chen, M. Van Hecke, Origami multistability: From single vertices to metasheets, Physical review letters, 114 (2015) 055503.
[14] H. Yasuda, T. Tachi, M. Lee, J. Yang, Origami-based tunable truss structures for non-volatile mechanical memory operation, Nature communications, 8 (2017) 1-7.
[15] K. Liu, T. Tachi, G.H. Paulino, Invariant and smooth limit of discrete geometry folded from bistable origami leading to multistable metasurfaces, Nature communications, 10 (2019) 1-10.
[16] K. Kuribayashi, K. Tsuchiya, Z. You, D. Tomus, M. Umemoto, T. Ito, M. Sasaki, Self-deployable origami stent grafts as a biomedical application of Ni-rich TiNi shape memory alloy foil, Materials Science and Engineering: A, 419 (2006) 131-137.
[17] S.A. Zirbel, R.J. Lang, M.W. Thomson, D.A. Sigel, P.E. Walkemeyer, B.P. Trease, S.P. Magleby, L.L. Howell, Accommodating thickness in origami-based deployable arrays, J Mech Design, 135 (2013).
[18] J.M. Skotheim, L. Mahadevan, Physical limits and design principles for plant and fungal movements, Science, 308 (2005) 1308-1310.
[19] S.N. Patek, W. Korff, R.L. Caldwell, Deadly strike mechanism of a mantis shrimp, Nature, 428 (2004) 819-820.
[20] S. Shan, S.H. Kang, J.R. Raney, P. Wang, L. Fang, F. Candido, J.A. Lewis, K. Bertoldi, Multistable architected materials for trapping elastic strain energy, Adv Mater, 27 (2015) 4296-4301.
[21] D. Restrepo, N.D. Mankame, P.D. Zavattieri, Phase transforming cellular materials, Extreme Mechanics Letters, 4 (2015) 52-60.
[22] R. Masana, S. Khazaaleh, H. Alhussein, R. Crespo, M. Daqaq, An origami-inspired dynamically actuated binary switch, Applied Physics Letters, 117 (2020) 081901.
[23] J.L. Silverberg, J.H. Na, A.A. Evans, B. Liu, T.C. Hull, C.D. Santangelo, R.J. Lang, R.C. Hayward, I. Cohen, Origami structures with a critical transition to bistability arising from hidden degrees of freedom, Nat Mater, 14 (2015) 389-393.
[24] T. Chen, O.R. Bilal, K. Shea, C. Daraio, Harnessing bistability for directional propulsion of soft, untethered robots, Proceedings of the National Academy of Sciences, 115 (2018) 5698-5702.
[25] T. Chen, J. Mueller, K. Shea, Integrated design and simulation of tunable, multi-state structures fabricated monolithically with multi-material 3D printing, Scientific reports, 7 (2017) 1-8.
[26] J.T. Overvelde, T. Kloek, J.J. D'haen, K. Bertoldi, Amplifying the response of soft actuators by harnessing snap-through instabilities, Proceedings of the National Academy of Sciences, 112 (2015) 10863-10868.
[27] S. Sengupta, S. Li, Harnessing the anisotropic multistability of stacked-origami mechanical metamaterials for effective modulus programming, Journal of Intelligent Material Systems and Structures, 29 (2018) 2933-2945.
[28] J.L. Silverberg, A.A. Evans, L. McLeod, R.C. Hayward, T. Hull, C.D. Santangelo, I. Cohen, Using origami design principles to fold reprogrammable mechanical metamaterials, Science, 345 (2014) 647-

650.
[29] J.N. Grima, R. Caruana-Gauci, M.R. Dudek, K.W. Wojciechowski, R. Gatt, Smart metamaterials with tunable auxetic and other properties, Smart Mater Struct, 22 (2013) 084016.
[30] K. Yang, S. Xu, J. Shen, S. Zhou, Y.M. Xie, Energy absorption of thin-walled tubes with pre-folded origami patterns: Numerical simulation and experimental verification, Thin-Walled Structures, 103 (2016) 33-44.
[31] H. Ye, J. Ma, X. Zhou, H. Wang, Z. You, Energy absorption behaviors of pre-folded composite tubes with the full-diamond origami patterns, Composite Structures, 221 (2019) 110904.
[32] J. Ma, Z. You, Energy absorption of thin-walled square tubes with a prefolded origami pattern—part I: geometry and numerical simulation, Journal of applied mechanics, 81 (2014).
[33] J. Song, Y. Chen, G. Lu, Axial crushing of thin-walled structures with origami patterns, Thin-Walled Structures, 54 (2012) 65-71.
[34] H.B. Fang, S.Y. Li, H.M. Ji, K.W. Wang, Dynamics of a bistable Miura-origami structure, Phys Rev E, 95 (2017).
[35] S. Li, K. Wang, Fluidic origami with embedded pressure dependent multi-stability: a plant inspired innovation, Journal of The Royal Society Interface, 12 (2015) 20150639.
[36] M.Z. Miskin, K.J. Dorsey, B. Bircan, Y. Han, D.A. Muller, P.L. McEuen, I. Cohen, Graphene-based bimorphs for micron-sized, autonomous origami machines, Proceedings of the National Academy of Sciences, 115 (2018) 466-470.
[37] S. Felton, M. Tolley, E. Demaine, D. Rus, R. Wood, A method for building self-folding machines, Science, 345 (2014) 644-646.
[38] Z. Zhao, J.T. Wu, X.M. Mu, H.S. Chen, H.J. Qi, D.N. Fang, Origami by frontal photopolymerization, Science Advances, 3 (2017).
[39] P.M. Dodd, P.F. Damasceno, S.C. Glotzer, Universal folding pathways of polyhedron nets, Proceedings of the National Academy of Sciences, 115 (2018) E6690-E6696.
[40] H. Melo, C. Dias, N. Araújo, Optimal number of faces for fast self-folding kirigami, Communications Physics, 3 (2020) 1-5.
[41] T.C. Hull, Modelling the folding of paper into three dimensions using affine transformations, Linear Algebra and its applications, 348 (2002) 273-282.
[42] S. Kamrava, D. Mousanezhad, H. Ebrahimi, R. Ghosh, A. Vaziri, Origami-based cellular metamaterial with auxetic, bistable, and self-locking properties, Scientific reports, 7 (2017) 1-9.
[43] C. Lv, D. Krishnaraju, G. Konjevod, H. Yu, H. Jiang, Origami based mechanical metamaterials, Scientific reports, 4 (2014) 1-6.
[44] X. Zhang, J. Ma, M. Li, Z. You, X. Wang, Y. Luo, K. Ma, Y. Chen, Kirigami-based metastructures with programmable multistability, Proceedings of the National Academy of Sciences, 119 (2022) e2117649119.